1 **Revision 2**

2

Constraints on aluminum and scandium substitution mechanisms in forsterite, periclase, and larnite: High resolution NMR

6

7 Ryan J. McCarty[1*], Jonathan F. Stebbins[1]

8 [1]Department of Geological Sciences, Stanford University, Stanford, CA 94305,

9 USA

10 *corresponding author, ryanjm@stanford.edu*

11

12 **ABSTRACT**

13 The incorporation of incompatible Al in forsterite is particularly interesting due to

14 its relevance in Al olivine-spinel geobarometry techniques as well as the proposed

15 influence of Al on upper mantle diffusion and water storage capacity. However,

16 determining the site preference and substitution mechanisms of aluminum in forsterite

17 presents considerable challenge, as the incompatibility of Al in the olivine structure

18 results in correspondingly low Al concentrations which are challenging to study. In this

19 work we use solid state Nuclear Magnetic Resonance (NMR) to directly observe Al

20 coordination in synthetic samples from which we can constrain site preferences. We

21 investigate Al in MgO and clinoenstatite to confirm that the forsterite spectra do not

22 contain contributions from these impurity phases. To better interpret our results we used

23 the Independent Component Analysis (ICA) algorithm, SIMPLISMA, which accurately

24 deconvoluted complex NMR line shapes, separating spectral components from known

25 impurities and enabling the identification of unknown spectral components which in

26 some cases we can assign to substituting Al. We additional investigate Al in larnite,

27 which has a tetrahedral environment similar to that of forsterite and which presents an

28 additional ICA test case, and investigate Sc in forsterite and periclase to add additionally

29 context to our Al observations. Our ^{27}Al and ^{45}Sc MAS NMR spectra place additional

30 constraints on the site preferences of Al in synthetic forsterite, clinoenstatite, periclase,

31 and larnite as well as Sc in forsterite and periclase.

32   In forsterite, we identified Al in the tetrahedral site and at least three distinct

33   octahedral environments. The overall ratio of contents of AlO_4 to AlO_6 is about 1:3; the

34   excess of the latter suggesting that at least two substitution mechanisms are necessary for

35   Al^{3+} incorporation in forsterite. In some cases the estimated species abundance for

36   observed features are as low as 70 µg/g Al^{3+}, but were readily detected by NMR. Also in

37   forsterite, we identified Sc in a single MgO_6 environment. In larnite (also known as belite

38   or C_2S in cement chemist notation), a single, ordered tetrahedral Al species is detected. In

39   enstatite samples, primarily composed of clinoenstatite, ^{27}Al NMR spectra look very

40   similar to previous observations of orthoenstatite, likely indicating a similar coupled

41   AlO_6 and AlO_4 substitution. In periclase, Al is observed in an undistorted MgO_6 site with

42   cubic or nearly cubic point symmetry, in addition to a lower symmetry, six-coordinated

43   site. This work provides new insight into incompatible element substitutions mechanism

44   in minerals, in forsterite's case indicating complex behavior involving multiple species

45   despite compositional simplicity.

46

47   **Keywords**: Forsterite, periclase, enstatite, larnite, belite, independent component

48   analysis, nuclear magnetic resonance, trace elements, SIMPLISMA

49   **INTRODUCTION**

50   Aluminum is an abundant element in Earth's mantle, but scarce in olivine, a

51   major mineral component of the upper mantle and a common phase in mafic rocks.

52   Despite aluminum's low concentrations in olivine (typically less than 400 µg/g), the

53   incorporation of incompatible Al^{3+} into olivine has drawn considerable interest due to its

54   relevance to a geobarometry technique (where Al^{3+} concentrations in olivine and spinel

55   are used to predict the equilibration pressure) (Wan et al. 2008; Coogan et al. 2014), its

56   proposed role in creating diffusion pathways for small ions, and its potential to generate

57   sites that could accommodate water in the upper mantle (Berry et al. 2007; Zhang and

58   Wright 2012).

59   In forsterite (Mg_2SiO_4), the magnesium rich end member of olivine, the preferred

60   lattice site of incorporated Al^{3+} is not obvious. The ionic radius of Al^{3+} (39 to 53 pm) and

61   its charge are between those of tetrahedral Si^{4+} (26 pm) and octahedral Mg^{2+} (72 pm)

62 (Shannon and Prewitt 1969). Due in part to this mismatch, the solubility of Al^{3+} in

63 forsterite is limited, with experimental work indicating a practical solid solution around

64 500 μg/g at temperatures between 1475 and 1390 °C (Grant and Wood 2010). This low

65 concentration limits the usefulness of diffraction methods to determine structural effects,

66 and can pose challenges of sensitivity for spectroscopic approaches. Many prior studies

67 of aluminum in forsterite have involved multi-dopant systems, and suggest a wide variety

68 of Al^{3+} incorporation mechanisms that are likely influenced by the presence or absence of

69 additional elements (Bershov et al. 1983; Purton et al. 1997; Berry et al. 2007; Evans et

70 al. 2008; Neuville et al. 2009; Zhang and Wright 2010). For example, Electron

71 Paramagnetic Resonance (EPR) measurements indicate charge balancing pairs of Cr^{3+}

72 and Al^{3+}, with the latter on the Si site (Bershov et al. 1983). From compositional

73 measurements, Al^{3+} was suspected to occupy both Si and M sites (Evans et al. 2008), and

74 later thought to be principally incorporated by disassociated charge balancing Si and M

75 site substitutions (Grant and Wood 2010). Computational atomistic simulations

76 referenced to previous vibrational spectroscopy have indicated that the site preference for

77 Al^{3+} is sensitive to both pressure and the charge balance mechanism, and can involve

78 both Si and M sites (Berry et al. 2007; Zhang and Wright 2010).

79   To investigate this question, we apply solid state nuclear magnetic resonance to

80 otherwise pure forsterite samples with trace Al^{3+}. Solid state NMR can have excellent

81 sensitivity, is selective to specific nuclides, and is capable of distinguishing coordination,

82 nearest and next nearest neighbors, deviations in symmetry, and/or changes in localized

83 charges, for favorable nuclides at concentrations as low as 0.01 to 0.1% (on an atomic

84 basis) (MacKenzie and Smith 2001; Stebbins and Xue 2014). At high Al concentrations,

85 ^{27}Al NMR can distinguish distinct Al octahedral sites with various Al or Si second

86 neighbors as well as detecting distorted and or disordered tetrahedral sites, as

87 demonstrated recently on Ca-Tschermak clinopyroxene, in which Al occupies a variety of

88 sites, as is likely in forsterite (Flemming et al. 2015). Although requiring longer

89 experimental acquisitions, NMR's capabilities persist at concentrations at or below 5

90 wt% Al_2O_3, as demonstrated by work that concluded that Al substitutes into

91 orthoenstatite via a Tschermak mechanism (Kohn et al. 2005).

92

Experimental challenges

93   Investigating an "incompatible" cation, such as Al^{3+}, by a bulk spectroscopic

94   method such as NMR can present a considerable challenge, in that Al^{3+} preferentially

95   partitions into other phases, which can mask detection of low concentrations of Al^{3+} in

96   the phase of interest. Equilibrating samples at high temperatures increases solubility, the

97   rate of diffusion, and decreases the time necessary to reach equilibrium, and thus is

98   advantageous. However, even when syntheses are carried out well below the minimum

99   melting temperature of the bulk system, trace impurities can induce localized melting. If

100   present, impurity phases, such as pyroxene or melt, can preferentially incorporate Al^{3+},

101   and only a small proportion of an Al^{3+} rich phase is necessary to overwhelm the spectra.

102   Despite the challenges of detecting low amounts of impurity phases, careful

103   characterization with Electron Probe MicroAnalysis (EPMA), X-ray mapping, and ^{29}Si

104   NMR, is useful to confirm sample quality, and to select materials for detailed

105   investigation by ^{27}Al NMR. The low Al^{3+} concentrations in olivine can require lengthy

106   NMR acquisitions, sometimes lasting 2-4 days.

108

Additional minerals investigated

110   We investigated Al containing periclase (MgO), because we intentionally added

111   excess MgO in our forsterite syntheses to prevent the formation of enstatite. Since

112   enstatite is known to incorporate low concentrations of Al, we also investigated Al

113   containing enstatite ($MgSiO_3$), enabling a direct comparison, and ruling out the

114   possibility of mistakenly assigning enstatite peaks as forsterite peaks.

115   To better understand the context of the resulting spectra of Al-containing

116   forsterite we also investigated similar systems. Al^{3+} in larnite (Ca_2SiO_4) was examined as

117   a system where Al occupies only tetrahedral sites. Similar to forsterite, larnite tetrahedra

118   are isolated from each other, linked only by divalent cations. Additionally, the maximum

119   concentration of Al in larnite is known to be much higher than that in forsterite, providing

120   an additional and higher concentration setting to more clearly demonstrate the

121   effectiveness of the SIMPLISMA algorithm discussed below. Lastly, we investigated

122   Sc^{3+} in forsterite and MgO. The charge of Sc is identical to that of Al, however the larger

4

123 ionic radius of Sc (octahedral Sc^{3+}, 73 pm) limits it to octahedral sites (Shannon and

124 Prewitt 1969).

125

126   **METHODS**

127 **Sample syntheses**

128   Unless otherwise noted, samples were synthesized by hand milling oxide powders

129 in isopropyl alcohol in an agate mortar, pressing dried material into a pellet, and heating

130 the material with intermittent additional milling and pellet pressing. All samples were

131 heated in platinum crucibles in air. Although equilibrium in a strict thermodynamic sense

132 is difficult to demonstrate in these types of experiments, we did confirm in most cases

133 that heating times were sufficient so that no further changes in Al speciation were

134 detectable, i.e. at least a steady state was obtained. With forsterite and periclase, we

135 found that the same Al speciation was reached, starting with Al in different initial phases

136 such as gibbsite, corundum, or spinel. Given the long, high temperature annealing times,

137 we assume that H_2O (and H^+) contents of the silicate phases are negligible in comparison

138 to Al concentrations. Minor, post-synthesis water or CO_2 absorption in MgO or CaO

139 would not be expected to affect the results reported here. For the most informative

140 samples whose spectra are described here, synthesis conditions and nominal

141 compositions are given in Table 1.

142   **Al^{3+} doped forsterite.** Al^{3+} doped forsterite was synthesized using various

143 reagents, with 1-3 wt% excess MgO to reduce the chance of formation of enstatite. We

144 mixed SiO_2 (Baker AR silica gel or quartz at 99.995% purity) and MgO (Baker AR MgO,

145 MgO at 99.99% purity, or MgO at 99.998% purity) with previously synthesized spinel

146 ($MgAl_2O_4$, made by sintering mixtures of MgO and alumina) or γ-$Al(OH)_3$. We hand

147 milled reagents in an agate mortar, the effects of which were undetectable, an alumina

148 mortar, which added unacceptable concentrations of alumina, or a zirconia mortar, which

149 added zirconia particles and contributed to glass formation. Several dozen samples were

150 heated at 1500 to 1650 °C for 72 to 240 hours, interrupted by 2 to 6 intermediate milling

151 steps. The most homogeneous samples as determined by EPMA and NMR are those

152 made by mixing forsterite with spinel, as in the spectra shown here. NMR spectra

153 indicated that most samples had reached a state of chemical equilibrium, or at least that

5

154   no further changes were occurring, before 200 hours at temperature. Forsterite samples

155   were difficult to crush and mill due to a relatively high fracture toughness of the heated

156   material. Intended Al^{3+} concentrations were 570 to 2700 µg/g.

157   **Al^{3+} doped periclase.** Al-periclase was synthesized from mixtures of 99.99%

158   purity MgO with small amounts of 50 nm particles of $Al(OH)_3$ (Nanostructured &

159   Amorphous Materials, Inc.) or spinel. Reagents were milled, pressed into pellets, and

160   heated, producing a dense ceramic that was difficult to subsequently mill. The nano-

161    $Al(OH)_3$ + MgO synthesis route reached steady state with respect to Al speciation in

162   approximately half the time required for the spinel + MgO route. Intended Al^{3+}

163   concentrations were 480 to 2100 µg/g.

164   **Al^{3+} doped clinoenstatite.** This phase was synthesized from Baker AR MgO,

165   dehydrated silica gel, and γ-$Al(OH)_3$, with excess SiO_2 (2 wt%) to avoid forsterite

166   formation. Synthesis temperatures were 1300 °C for 96 to 144 hours with 1 to 3

167   intermediate milling steps. In subsequent firings, clinoenstatite grain growth was

168   minimal, and the samples crushed and milled easily.

169   **Al^{3+} doped larnite.** Larnite was synthesized from mixtures of $CaCO_3$, SiO_2, and

170   γ-$Al(OH)_3$. Reagents were sintered for 90 minutes at 1450 °C after milling, reground, and

171   sintered for 60 hours at the same temperature. After a number of preliminary

172   experiments, impurity phases were found to be minimized (although still present) when

173   Si was replaced by Al on an equimolar basis, with nominal bulk Al contents of 0.15 and

174   0.53 wt%.

175   **Sc^{3+} doped forsterite.** As for Al-forsterite, Sc-forsterite with excess MgO (3

176   wt%) was synthesized from Baker AR MgO, Baker AR silica gel and 99.95% pure

177   Sc_2O_3. Mixed reagents were heated for a total of 192 hours at 1500 °C, with two

178   intermediate milling steps. Intended Sc^{3+} concentrations were 1350 to 3350 µg/g.

179   **Sc^{3+} doped periclase.** Several syntheses resulted in samples containing periclase

180   with NMR-observable Sc contents. In one approach, 99.99% purity MgO and 99.95%

181   purity Sc_2O_3 were mixed in a 50/50 ratio by weight and heated at 1300 ˚C to 1500 ˚C for

182   24 to 72 h, yielding only Sc-doped periclase and Sc_2O_3. Heated samples formed dense

183   ceramics that were difficult to subsequently mill. A second type of sample resulted from

184 a Sc-doped forsterite mixture with a bulk Sc_2O_3 content of 1.6 wt% and a large excess in

185 MgO (70 wt%), heated at 1280 ˚C for 72 h.

186

Electron Probe Microanalysis (EPMA)

188   Electron probe microanalysis characterizations were performed using a JEOL

189 JXA-8230 instrument. X-ray intensities were routinely standardized to a synthetic single

190 crystal forsterite (Mg and Si), corundum (Al), kyanite (Al) and Sc metal (Sc).

191 Additionally San Carlos olivine (Mg, Si, and Fe), spessartine garnet (Al), wollastonite

192 (Ca and Si), albite (Na, Al and Si), and hematite (Fe), were intermittently used as

193 secondary standards. A voltage of 15 kV, 20 nA current, 2 μm spot size, and count times

194 of 4 minutes were used. Reference material of synthetic, Al-free forsterite was used to

195 determine background noise levels when analyzing low Al concentrations. Water

196 sensitive MgO and CaO samples were encapsulated in an epoxy round, cured, dry

197 polished on silicon carbide sand papers down to 2000 grit, and then stored with desiccant

198 in a vacuum; exposure to air was limited to 10-15 minutes.

199   Backscattered electron (BSE) images with high contrast ratios, energy dispersive

200 spectroscopic (EDS) and wavelength dispersive spectroscopic (WDS) maps were used to

201 locate sample heterogeneities, such as scarce aluminum-rich glass and crystalline

202 impurities, when present. Major element concentrations were generally within

203 experimental error of nominal values for the analyzed phases and are thus not reported.

204 Element totals were typically within $\pm$ 0.03 wt%, and the largest individual major

205 element variation we identified was $\pm$ 2 wt% of the expected value.

206   For high concentration elements, we determined that the observed variations in

207 composition (Mg or Si) were randomly distributed and not correlated to sample trace

208 concentrations. Data were rejected when low totals indicated problems with the carbon

209 coating, focus, polish, or other difficulties.

210

NMR Spectroscopy

212   Samples were prepared for solid-state MAS NMR by crushing into 2-20 μm

213 powders. A single 3.2 mm ZrO_2 rotor with a low ^{27}Al background signal was used for the

214 entirety of the project and was spun at 20 kHz. There was no detectable ^{45}Sc background

7

215   signal. Packed sample mass was typically 30 to 40 mg. Spectra were collected with a 14.1

216   Tesla Varian Unity/Inova 600 MHz spectrometer (^{27}Al at 156.25 MHz, ^{45}Sc at 145.98

217   MHz) and an 18.8 T Varian Unity/Inova 800 MHz spectrometer (^{27}Al at 208.40 MHz,

218   ^{45}Sc at 194.64 MHz) using Varian/Chemagnetics "T3" MAS probes. For ^{27}Al spectra, 0.1

219   M aqueous $Al(NO_3)_3$ was referenced to 0 ppm and was used for power level

220   determinations. Effective radiofrequency power of 103 kHz was determined by

221   measuring the 360˚ tip angle for the liquid standard. A 0.28 μs pulse, ideally a 30˚ tip

222   angle for this nuclide in solids with significant quadrupolar coupling, was used.

223   Referencing was reproducible to within ± 0.13 ppm. ^{45}Sc spectra were referenced to a

224   dilute aqueous solution of $ScCl_3$. Effective radiofrequency power of 125 kHz was

225   determined by measuring the 360˚ tip angle for the liquid standard. A 0.163 μs pulse,

226   ideally a 30˚ tip angle for this nuclide in solids with significant quadrupolar coupling, was

227   used.

228   Short pulse delays of 0.1 s for ^{27}Al or 0.2 s for ^{45}Sc were preferred to maximize

229   the signal to noise ratios and minimize data collection times. Spectra shown here are

230   typically not fully relaxed, but in general, differential spin-lattice (T_1) relaxation among

231   spectral components was not noticeably different in noisy spectra collected with longer

232   delay times. Despite incomplete characterizations of relaxation, we still believe these

233   peak areas to be meaningful, as species within the same material (i.e. tetrahedral and

234   octahedral Al in forsterite) are expected to relax at equal rates, and approximate peak area

235   ratios between intended and impurity phases are sufficient for our discussion.

236   ^{27}Al NMR rotor background signal was removed when needed by subtracting a

237   simulated (noiseless) background spectrum based on modeling of multiple experimental

238   spectra of the rotor, a procedure that reduces the noise of the difference spectrum

239   considerably. Simulated background corrections agree within the noise level with

240   background corrections based on subtraction of experimental FID's.

241

242   **Additional sample characterization**

243   Sample homogeneities and phase identities were also investigated on powdered

244   samples using a Rigaku Geigerflex powder X-ray diffractometer and ^{29}Si MAS NMR

245   collected with a 9.4 T Varian Infinity Plus 400 MHz spectrometer (^{29}Si at 79.42 MHz).

8

246

247 **NMR data Analysis**

248   To help interpret our NMR data, an independent component analysis (ICA) was

249 used, which determines statistically independent subcomponents to describe a larger

250 parent data set. ICA techniques, although relatively uncommon in solid state NMR, are

251 more commonly used with liquid state NMR and other spectroscopic techniques, such as

252 IR/Raman, fluorescence, and UV-vis. Similar algorithm-based analysis techniques, such

253 as evolving factor analysis (EFA) and principal component analysis (PCA), have even

254 wider spread spectroscopic applications, including interpreting NMR spectra of inorganic

255 materials (Mason et al. 2012, 2016), deconvolution of liquid state NMR spectra

256 (Stoyanova et al. 1995; Stoyanova and Brown 2001), and analyzing Raman spectra of

257 alkali silicate glasses (Zakaznova-Herzog et al. 2007). We also tested both EFA and PCA

258 methods for our spectra but they did not produce reasonable components to describe

259 known quadrupolar peak shapes.

260   In this study we used the SIMPLe-to-use Interactive Self-modeling Mixture

261 Analysis (SIMPLISMA), which was previously found to perform well relative to other

262 ICA's on liquid-state NMR spectra (Monakhova et al. 2014). SIMPLISMA determines

263 independent components on the basis of standard deviations, under the assumption that

264 more significant independent components will have larger standard deviations than less

265 significant components. Readers are directed to the following references for concise

266 presentations of the theory and supporting formula of SIMPLISMA (Windig and

267 Guilment 1991; Windig et al. 2002). Versions of the code can be readily found online and

268 is detailed in Windig's 1997 publication (Windig 1997; Mathworks.com 2007). A tutorial

269 demonstrating the code on NMR data is also available (Solidstatenmr.com 2017). In our

270 samples, differences in aluminum concentration, heating times, and other variations in

271 sample synthesis provided sufficient variability among spectra to allow multiple different

272 components to be obvious, but generally highly overlapped. For each mineral, we found

273 that analyzing different combinations in subsets of all of the spectra collected was useful

274 for determining the most accurate and chemically relevant independent components,

275 which were persistently determined regardless of specific spectra used. We found that the

276 number of independent components necessary to describe the spectra, a user specified

277   value, was easy to determine iteratively, with excessive components typically making

278   very small contributions or describing only noise or differences in phasing, as was

279   previously reported (Monakhova et al. 2014).

280   As discussed in detail later, for our spectra, SIMPLISMA was capable of deriving

281   components identical to spectra for known impurity phases, such as spinel. SIMPLISMA

282   most accurately determined known impurity phases when the spectra were windowed to

283   exclude spinning sidebands and the intensity of all spectra were individually normalized

284   to their maximum and minimum values. When sidebands were included, the algorithm

285   correctly associated sidebands with central peaks; however, the overall accuracy of

286   determining components typically suffered as the window width increased.

287   Fitting of spectra with quadrupolar line shapes was done using DMFit2015

288   (Massiot et al. 2002).

RESULTS

Aluminum in forsterite (Mg_2SiO_4)

291   In our samples, EPMA showed that aluminum is present in both the forsterite

292   crystals and in an intergranular glass phase. In the forsterite grains, EPMA compositions

293   (in the range of 120 to 1800 μg/g) were consistently only 20 to 35% of the intended,

294   weighed-in Al^{3+} concentrations, suggesting that significant Al was present in Al-rich

295   impurity phases of low abundance. However, across all samples, analyzed forsterite Al

296   concentrations were observed to vary systematically with intended bulk composition. Al

297   contents typically varied by about 18% (relative) among different forsterite grains in a

298   given sample, but individual grains were typically homogeneous within the noise level.

299   The measured Al^{3+} concentrations are above our ^{27}Al NMR detection limit which we

300   estimated to be about 25 μg/g in a typical 35 mg forsterite sample, based on assumptions

301   of a peak with a FWHM less than 8 ppm, 80% relaxation with a pulse delay of 1 s and a 6

302   day acquisition.

303   A scarce glass phase was also detected in many samples, located along grain

304   boundaries or at triple junctions, as visible for a relatively glass-rich sample in Figure 1.

305   The abundance of glass and its composition corresponded somewhat with the purity of

306   reagents used, but was present in small amounts even in the highest purity experimental

10

307   products. Analysis of the glass was challenging, as such regions were typically smaller

308   than the EPMA beam size, but indicated highly varied compositions rich in Si, Al, Mg,

309   and Ca, with Al_2O_3, concentrations between 1.1 to 12.4 wt%. The glass compositions did

310   not correspond to that of any known mineral. Despite its low abundance, the glass is

311   expected to produce a sizeable feature in the ^{27}Al NMR spectra due to its high Al

312   concentration relative to the forsterite.

313   Small amounts of spinel were detectable in samples heated for shorter durations.

314   In one sample out of 18 studied by EPMA, we also detected grains with enstatite

315   composition, and correspondingly, the ^{27}Al NMR spectra of this particular sample

316   resembled a mechanical mixture of Al-doped forsterite and Al-doped enstatite. Despite

317   all samples being synthesized with excess MgO, periclase was never detected by EPMA,

318   possibly because it retained a similar small grain size to pure MgO samples and/or was

319   hydrated and subsequently removed during the wet polishing process.

320   In the ^{29}Si NMR spectra of our most completely reacted samples, we could detect

321   only forsterite, and spectra were identical to the aluminum free material, i.e. the signal

322   from any glass that was present was too low in intensity to be detected. Powder XRD of

323   the samples detected only forsterite.

324   The ^{27}Al NMR spectra contained multiple narrow AlO_6 features between 11 and -

325   3 ppm with possible underlying broader components, and broad AlO_4 features between

326   95 and 20 ppm with smaller AlO_5 components at the lower end of this range. Some

327   features were clearly identifiable, such as unreacted spinel when present, which produced

328   an AlO_4 peak centered at about 69 ppm and an AlO_6 peak centered at about 12 ppm in a

329   roughly 1:8 intensity ratio. Other features, such as the broad AlO_4 and AlO_5 components,

330   appear to be composed of at least three aluminum species; however, determining the

331   relative contribution of each component was difficult. Examples of typical spectra are

332   presented in Figure 2, Figure 3, and the 1500 °C sample in Figure 4.

333   As detailed below, the spectra for the Al-doped forsterite samples are unique and

334   distinct from those for MgO and for enstatite. The characteristic very narrow AlO_6 peak

335   for Al-MgO is absent, and while some of the data do resemble those for enstatite (Fig. 2),

336   comparisons between carefully referenced spectra indicate unique AlO_6 components for

337   each material. This is especially obvious in 18.8 T spectra, where the enstatite peak

11

338   maximum (at -1.1 ppm) appears at a peak minimum in the forsterite samples, between

339   peaks at 2.0 and -2.2 ppm.

340   SIMPLISMA consistently determined that there are only three significant,

341   independent components in these spectra (Fig. 3). Inputs included background subtracted

342   spectra from 14.1 or 18.8 T, with as few as 6 and as many as 21 spectra. The specific

343   input spectra used influenced the edges of peaks and neighboring baselines, but

344   minimally affected the derived component peak areas and shapes. The easiest to interpret

345   result is component 2, which conforms to known spectra for spinel. The deconvolution of

346   a spinel component, which was known to be present as incompletely reacted starting

347   material in some of our samples, is a testament to the effectiveness of the SIMPLISMA

348   algorithm. Component 3 has a peak shape, width, and position containing AlO_4 and AlO_5

349   components that closely resemble those typical of Ca- and Al-containing silicate glasses

350   at compositions known by EPMA measurements to be present in our samples (Neuville et

351   al. 2008). In comparisons among samples, the relative peak area of this glass-like feature

352   approximately correlates with the abundance of Al-rich intergranular phases observed in

353   EPMA when measured Al concentrations were taken into account.

354   In contrast, component 1 is unique to the forsterite samples, and indicates that the

355   area of the higher frequency AlO_4 feature is correlated to that of the AlO_6 peaks,

356   suggesting that they are indeed all part of the same phase. The relative peak area of

357   component 1 averages 20-40% of the total area, which approximately agrees with the

358   EPMA-measured forsterite composition and the intended bulk sample composition (20 to

359   35% of the total Al in forsterite and the remainder in other phases). Relative peak areas

360   from component 1 determined from 14.1 and 18.8 T spectra indicate that approximately

361   25 to 27% of the Al^{3+} incorporated into the forsterite structure is tetrahedral and 72 to

362   75% is octahedral.

363   The AlO_6 contribution to the derived component 1 is complex, typically with

364   three or four peak maxima even in samples that are free from AlO_6 containing impurity

365   phases, such as spinel. The line shapes are different for spectra collected at 14.1 and 18.8

366   T, because of the reduced effects of quadrupolar coupling at the higher magnetic field.

367   Quadrupolar coupling can produce split peaks with two maxima when both the coupling

368   constant C_Q is large enough and the asymmetry parameter η is small enough,

12

369   complicating data analyses. Using quadrupole line shapes generated in DMFit2015 we

370   were able to fit original datasets from both fields with multiple quadrupolar line shapes

371   that reproduced the spectra reasonably well (Massiot et al. 2002). But, due to limited

372   fitting constraints, in part because of overlapping peaks and noise, we could not derive a

373   set of unique parameters or relative peak areas. We are confident, however, that a

374   minimum of three distinct types of AlO_6 sites are required to explain the spectra.

375   We also conducted a preliminary investigation of the effect of temperature on

376   Al^{3+} site occupancies in forsterite. Sample material that had been heated for 168 hours at

377   1500 °C and quenched (which produced typical spectra as in Figs. 2 and 3) was then

378   heated for an additional 72 hrs at 1200 °C. The lower temperature sample (Fig. 4) shows

379   a decreased amount of the glass phase (at least as represented by its contained Al),

380   indicating some crystallization, and increased intensities for both the higher frequency

381   tetrahedral component (at about 75-95 ppm) and the higher frequency octahedral peak (at

382   about 10 ppm). In other samples, the changes in the glass peak area with temperature are

383   often minimal, with the most obvious changes among the various octahedral components.

384

Aluminum in periclase (MgO)

386   EPMA measurements of Al-doped MgO samples indicate concentrations within

387   one standard deviation of the intended values. No glass or other impurity phases were

388   detected, possibly because of the small grain size of less than about 3 μm.

389   The ^{27}Al NMR spectra contain a remarkably narrow (FWHM 0.14 ppm), fast

390   relaxing peak near the high frequency extreme of the known AlO_6 region (about 16 ppm),

391   a neighboring lower frequency AlO_6 peak (shoulder at 14.2 ppm), an underlying broad

392   AlO_6 feature, and a broad four coordinated resonance(s) between 90 and 40 ppm (Fig. 5).

393   Time-temperature studies indicated that equilibrium, or at least steady state, was reached

394   by 68 hours at 1500 ˚C. Samples heated for shorter durations or heated at lower

395   temperatures had obvious spinel peaks in the spectra, as well as an unexpected

396   intermediate phase Gaussian shaped peak centered at 82 ppm. This intermediate feature

397   was only detected, and was always detected, when both spinel and Al in MgO were both

398   present in the sample. Figure 5 illustrates the ^{27}Al NMR spectra of an equilibrated MgO

399   sample.

13

400   Due to its fast relaxation of the remarkably narrow peak, this feature should be

401   easily identifiable if present in spectra of Al-forsterite and other minerals. The area of the

402   narrow peak typically represents 8 to 18% of the total octahedral intensity; its width

403   requires a very small quadrupolar coupling parameter C_Q no larger than 0.45 MHz (Table

404   2). The C_Q is likely less than this value, as the observed 180° radiofrequency pulse width

405   of 5.0 μs is nearly the same as that for the liquid standard, which also requires a very low

406   C_Q value. In solids, the small C_Q is indicative of a high symmetry with a cubic or nearly

407   cubic point symmetry, which we believe is due to Al^{3+} in the Mg^{2+} site, undistorted by

408   nearby vacancies or additional Al/Mg substitutions. Its high frequency peak location also

409   implies relatively short bond lengths for octahedral aluminum, likely an effect of

410   localized charge compensation and the Al^{3+} cation in an Mg^{2+} site. The other AlO_6 and

411   AlO_4 features in the spectra, which must originate from lower symmetry chemical

412   environments, are discussed in more detail in McCarty (2016), as are additional

413   observations on Al in periclase.

414

415   **Aluminum in enstatite ($Mg_2Si_2O_6$)**

416   We attempted to avoid formation of enstatite in our forsterite samples by adding

417   excess MgO to all, and quenching some from temperatures above those at which enstatite

418   is stable. However, to directly compare our forsterite spectra to that of a potential

419   enstatite impurity, we synthesized Al-enstatites with mixing and milling procedures

420   identical to those for our most fully-reacted forsterites, although with different

421   proportions of reagents and lower temperatures.

422   ^{29}Si NMR indicated that about 70 to 80% of each sample was composed of

423   clinoenstatite. The remaining materials included mixtures of protoenstatite,

424   orthoenstatite, and minor amounts of cristobalite (SiO_2). Glass was not detected in these

425   spectra. EPMA analysis indicated sparse, unreacted SiO_2 in a matrix of fine-grained (< 20

426   μm) enstatite containing Al at concentrations 15 to 60% below the intended syntheses.

427   We noted large heterogeneities in Al concentration, with the majority of values clustered

428   around the mean but some concentrations at twice the mean value. Additional heating led

429   to minimal increases in homogeneity, implying slow intergranular Al transport relative to

430   that in our forsterite experiments at higher temperatures. We were not confident that

14

431   detecting intergranular glass by EPMA was possible due to the small grain size and

432   difficulties with polishing the grain mounts.

433   ^{27}Al NMR spectra of Al-doped enstatite (one example in Fig. 2), contain a broad

434   AlO_4 peak with narrow AlO_6 components, as well as signal from unreacted spinel. Our

435   spectra are similar to those in previous investigations of anhydrous orthoenstatites with

436   much higher Al contents, with AlO_6 peaks nearly identical (Kohn et al. 2005). The four

437   coordinated regions of our spectra also appear to contain a glass peak similar to the

438   forsterite component 3 and to previously studied aluminosilicate glasses (Neuville et al.

439   2008): it is not clear how much, if any, of this component is actually in the pyroxene.

440   Although the enstatite spectra look similar to those of our forsterite samples, at

441   18.8 T, the enstatite AlO_6 peak maximum is clearly in between those of the forsterite, as

442   visible in Figure 2. This is further supported by spectra acquired at 14.1 T, where the

443   enstatite peak maximum is consistently 2 ppm higher than the forsterite peak maximum.

444   In the forsterite spectra used for our analyses of Al components, we thus believe that

445   there is little to no enstatite component.

446

447   **Aluminum in larnite ("belite," β-Ca_2SiO_4)**

448   Synthesis of Al-doped samples of larnite without significant Al-rich impurity

449   phases was not successful. The most interpretable data were for samples made by

450   replacing Si with Al on an equimolar basis with total bulk Al contents of 0.15 or 0.53

451   wt%. In the latter sample, EPMA imaging detected rounded, 40 to 60 μm grains that

452   contained 40% of the intended total Al. Thin regions of intergranular glass (42 wt%

453   Al_2O_3, 44 wt% CaO, and 12 wt% SiO_2) were common. X-ray diffraction, optical

454   microscopy and ^{29}Si NMR data indicated that the crystalline components of these

455   samples were nearly all larnite, with a few percent of the γ-Ca_2SiO_4 phase.

456   The ^{27}Al spectra of our samples contain peaks only for AlO_4 species (Fig. 6).

457   Most of the components of the spectra are relaxed using a 0.1 s delay time, with a small

458   amount of additional intensity related to the highest frequency peak present in 1 s delay

459   time spectra. Using both 14.1 and 18.8 T spectra of our samples we determined the

460   parameters for the prominent, high frequency peak with a clear quadrupolar lineshape

461   (Table 2, Fig. 6).

462   SIMPLISMA analysis of multiple spectra of larnite samples determined 4

463   components. Component 1 describes the high frequency quadrupolar lineshape,

464   component 2 is very similar to data on Al^{3+} in alite (Ca_3SiO_5), component 3 resembles a

465   typical calcium aluminosilicate glass, and component 4 is the expected rotor background

466   signal which was subsequently subtracted and is not shown. Because components 2, 3

467   and 4 can be attributed to impurity phases, it can be concluded that component 1

468   originates from Al in ordered tetrahedral sites in larnite. Using a least squares regression

469   to fit component 2, component 3, and our simulation of component 1 to the spectra of the

470   "larnite 0.53%" sample, we determined that $41\% \pm 4$ of the total intensity was from Al in

471   the larnite, in good agreement with our EPMA measurements (40%).

472   As reported by Skibsted et al. (1994), we confirm that only AlO_4 species are

473   necessary to accommodate Al^{3+} in larnite. For unknown reasons, our observed peak is

474   about half the width of that previously reported, resulting in different derived parameters.

475   Due to the good agreement between the EPMA-determined concentrations and the

476   relative area of the well-defined quadrupolar doublet, we suspect there is minimal, if any,

477   disordered AlO_4 in larnite.

478

Scandium in forsterite

480   EPMA on our Sc-doped forsterites indicates homogeneous samples with no other

481   mineral or glass phases detected by BSE imaging, EDS, or WDS mapping. Point analyses

482   indicated higher homogeneity within individual grains (sample standard deviations of 45

483   to 70 µg/g Sc) and lower homogeneity between grains (sample standard deviations of 130

484   to 270 µg/g Sc). Despite the apparent homogeneity, the observed concentrations were

485   below the expected synthesis values by an average of 14%.

486   In the ^{45}Sc NMR spectra of Sc-forsterites, a single, well-defined quadrupolar peak

487   shape is present in the range typical for ScO_6 sites (Fig. 7). This peak and the parameters

488   derived from both 14.1 and 18.8 T data (Table 2) do not resemble previously reported

489   spectra for known scandium phases, such as the Sc_2O_3 synthesized at the same

490   temperature (Sc_2O_3 has two distinct Sc octahedral sites and its spectrum correspondingly

491   has two overlapped quadrupolar powder patterns) (Kim et al. 2006). The spectra for

492   forsterite samples containing both lower and higher Sc concentrations are identical except

16

493   for amplitude. The calculated peak shape agrees well with the experimental spectra and

494   also accurately reproduced observed spinning sidebands (not shown).

495

496   **Scandium in periclase**

497   In reacted mixtures of MgO and Sc_2O_3, we detected a peak which is clearly

498   different than Sc in forsterite, appearing as a low intensity, narrow feature at 210 ppm

499   due to a high symmetry site, with a FWHM peak width of only 0.4 ppm, and thus a

500   maximum C_Q of < 1.5 MHz (Fig. 8). On the basis of the similarly narrow peak width of

501   AlO_6 in MgO and its relatively high frequency, we assign this peak to Sc^{3+} in an MgO_6

502   site with cubic or nearly cubic point symmetry. A similar peak was seen in a mixed

503   periclase-forsterite sample ("Sc-MgO 1.6%"), the spectrum of which also showed Sc in

504   the forsterite as described above. All Sc-MgO samples contained a large excess of the

505   Sc_2O_3 phase, whose NMR peak intensity served as a rough internal standard for rough

506   estimates of the concentration of Sc in the periclase, as noted in Table 1.

507   A $MgSc_2O_4$ phase was reported to form at temperatures above 2000 ˚C (Muller-

508   Buschbaum 1966), but our synthesis conditions yielded only mixtures of Sc_2O_3 and MgO

509   containing trace amounts of Sc^{3+}.

510   **DISCUSSION**

511   The identification of a spectral component that is clearly Al in forsterite provides

512   new and unique constraints on Al^{3+} site preference and substitution mechanisms. These

513   results also demonstrate the possible complexity of even this "simple", single-element

514   substitution into olivine. Spectral component 1 (Fig. 3) does contain both AlO_4 and AlO_6

515   peaks, indicating Al^{3+} substitution into both Si and M sites, and suggesting that a

516   conventional Tschermak's mechanism (Evans et al. 2008; Grant and Wood 2010) ($^{IV}Si^{4+}$

517     $+ {}^{VI}Mg^{2+} = {}^{IV}Al^{3+} + {}^{VI}Al^{3+}$) does play an important role . However, the roughly 1/3

518   ratio of tetrahedral to octahedral Al peak areas suggests that one or more additional

519   mechanisms are also operating, to allow substitution of excess Al as AlO_6. Such

520   mechanisms have been proposed, and in the absence of other substituting cations, it is

521   generally thought to involve charge compensation with one Mg^{2+} vacancy for every two

522   incorporated Al^{3+}. Our results do not yet allow all such details to be refined, but the clear

17

523   presence of multiple AlO_6 sites does suggest important complexity. Furthermore,

524   preliminary studies indicate that the proportions of different Al^{3+} species may be

525   influenced by temperature.

526   The component 1 AlO_4 peak for the forsterite is somewhat broad and without a

527   clear quadrupolar line shape, which could be the result of low signal-to-noise or to some

528   disorder leading to distributions of NMR parameters. However, its location is at the high

529   frequency extreme (left side as plotted) of the known range for such sites in minerals,

530   with allowable isotropic chemical shifts bounded by at least 95 ppm as defined by the

531   upper side of this component (Stebbins 1995). This result is not surprising, as SiO_4

532   groups in forsterite have one of the highest ^{29}Si chemical shifts known for diamagnetic

533   silicates (-62 ppm), as expected for Q^0 groups (no shared oxygen between tetrahedra)

534   (Stebbins 1995).

535   Further insight into Al^{3+} substitution can be gained by comparing forsterite to

536   larnite, which has the same stoichiometry and similar topology, with Q^0 Si sites and

537   larger M sites with distorted 6 or 7-fold coordination (Jost et al. 1977). Despite the

538   apparent lack of substitution of Al^{3+} into the too-large Ca sites in larnite, the overall

539   solubility appears to be higher than in forsterite. AlO_4 sites in larnite also produce an

540   extreme ^{27}Al isotropic chemical shift of 96 ppm, but appear to be highly ordered with a

541   well-defined quadrupolar line shape (Fig. 6). These differences are possibly related to the

542   absence of octahedral Al^{3+} in this mineral and its influence on the substitution

543   mechanisms and cation distributions. In larnite, the Al^{3+} species is probably either always

544   isolated from, or always neighboring, the defect providing the charge balance, leading to

545   the observed ordered line shape. This contrasts strongly with forsterite, where there are

546   many more conceivable variations in nearest cation neighbors for a tetrahedral site,

547   including Mg^{2+}, Al^{3+}, or vacancies in the M1 and/or the M2 sites. Each of these

548   combinations would be expected to affect the chemical shift or quadrupolar parameters,

549   producing peaks the sum of which could resemble the broad AlO_4 feature visible in

550   component 1 derived from our forsterite spectra. It is also possible that due to the

551   presence of neighboring M site occupants, the AlO_4 site symmetry might be distorted

552   resulting in greater C_Q values and a broader peak.

18

553 Based on attempts at lineshape fitting, the complexity of the forsterite component

554 1 AlO_6 peak shapes requires three (or more) distinct sites. The three species represent

555 different local environments, possibly Al^{3+} in M1 vs. M2, or the effects of a vacancy or

556 of Al^{3+} in a neighboring M site or of Al^{3+} in an adjacent Si site. Any of these could cause

557 variations in the chemical shift, C_Q, or quadrupolar asymmetry parameter η, leading to

558 changes in peak shape and position.

559 Previous ^{25}Mg NMR investigations of pure forsterite showed that the two M sites

560 have distinct NMR peak parameters that can potentially be compared to our ^{27}Al results

561 (Table 2) (Davis et al. 2010). This provides an opportunity to consider the effects of

562 cation substitution on site distortion. The quadrupolar coupling constant C_Q is

563 proportional to the principle value of this tensor and to the nuclide-specific quadrupolar

564 moment Q (MacKenzie and Smith 2001). The reported ^{25}Mg C_Q values of 5.2 MHz (M1)

565 and 4.3 MHz (M2) can thus be adjusted for ^{27}Al by multiplying by the ratio of Q's for the

566 two nuclides (147/199) (MacKenzie and Smith 2001), yielding predicted values of 3.8

567 and 3.2 MHz. These are among the range of values that produce reasonable line shapes

568 for the latter nuclide in forsterite.

569 Our ^{45}Sc NMR results for Sc-forsterite also provide some perspective on Al^{3+}

570 substitution. The much larger size of the Sc^{3+} cation (73 vs. 53 pm for six-fold

571 coordination) precludes its substitution into tetrahedral sites, consistent with the observed

572 single ScO_6 NMR signal with a well-defined quadrupolar lineshape. As for AlO_4 groups

573 in larnite, the lack of peak broadening due to disorder suggests that all detectable Sc^{3+}

574 sites in forsterite are equivalent, and thus are either uniformly associated with or

575 uniformly disassociated from whatever defect is providing charge compensation, for

576 example a Mg^{2+} vacancy.

577 Adapting the reported ^{25}Mg NMR data for forsterite (Davis et al. 2010) to ^{45}Sc

578 again requires multiplying the C_Q's by the ratio of the magnitudes of the quadrupolar

579 moments, which in this case is 220/199. The predicted values of 5.7 and 4.8 MHz are

580 very different from our observed single C_Q value for the ScO_6 site (9.4 MHz), suggesting

581 in this case that considerable additional site distortion occurs. Again, comparison with the

582 ^{27}Al data for AlO_6 sites in forsterite highlights the complexity of the substitution

19

583 mechanism(s) in the latter as well as the ability of NMR to identify a single trace cation

584 substitution mechanism when such simplicity is actually present.

585   Our preliminary studies also suggest that octahedral site occupancies for Al in

586 forsterite may change significantly with temperature, but further experiments will be

587 needed at the lower temperatures to allow confirmation of re-equilibration under

588 conditions of slow Al diffusion and/or exsolution.

589   **IMPLICATIONS**

590   Despite the difficulties of producing single-phase samples doped with

591 incompatible elements and the unexpected complexity of some of the resulting spectra,

592 we have demonstrated that spectroscopy on multiple related samples with varying phase

593 proportions, combined with EPMA characterization and SIMPLISMA data analysis, can

594 constrain the substitution mechanisms for Al^{3+} in forsterite. Experiments that examine

595 Al^{3+} sites in other minerals with analogous tetrahedral and octahedral sites (e.g. larnite,

596 periclase, and CaO) and the analogous but larger trivalent cation Sc^{3+} are also helpful in

597 interpreting spectra, as well as in showing that when trace element substitution does

598 occur by a simple, single mechanism, that process can be readily and definitively

599 observed. In line with its success for NMR spectroscopy of organic molecular liquids,

600 SIMPLISMA can perform well at separating complex, overlapped solid state NMR

601 spectra into components, which can then be more easily given structural significance.

602   Our results for Al in forsterite suggest that more than one substitution mechanism

603 plays a role at the same time and experimental conditions, with charge compensation on

604 tetrahedral and octahedral sites important but excess AlO_6 also present, necessarily

605 accompanied by other means of charge balance. The balance of these different

606 mechanisms may shift with temperature and compositional variables. Several of the

607 substitutions proposed in the literature (Purton et al. 1997; Grant and Wood 2010; Zhang

608 and Wright 2010) may well operate simultaneously, a realization supported in part by the

609 established pressure sensitive nature of Al concentrations (Wan et al. 2008). Future work

610 on trace element substitution and solubility should recognize the potential for multiple

611 co-existing mechanisms. The success, albeit with long hours of spectrometer time, for

612 samples with low Al concentrations bodes well for future studies of this and other NMR-

613 accessible trace elements in silicate minerals. Future work at higher magnetic fields could

20

614   provide much needed gains in spectral resolution and sensitivity. Potentially, more

615   complex NMR techniques such as Al-Al homonuclear correlation experiments may

616   provide an additional level of understanding of trace element incorporation (Iuga 2011).

617   Our results for other minerals, although discussed only briefly here, have wider

618   implications as well. The narrow NMR peak width for the undistorted Al^{3+} site in MgO,

619   paired with the simple crystal structure, provides a model system that may prove useful

620   for studies of solid state synthesis reactions.

621   For larnite, our work confirmed previous findings of solely tetrahedral aluminum

622   (Skibsted et al. 1994). Due to this mineral's high relevance to the cement industry, our

623   reported peak parameters, and the concept of using an ICA to determine independent

624   components from complex spectra, may help develop tools for accurately characterizing

625   complex multi-component cements.

626   Our investigations of trace contents of Sc^{3+} again mark this cation as an excellent

627   spectroscopic target representing the behavior of a trivalent cation with radius between

628   those of Al^{3+} (smaller) and the rare earth cations (larger), as previously demonstrated for

629   Sc-doped pyrope and grossular garnets (Kim et al. 2007). Its ready detectability, wide

630   chemical shift range, and convenient quadrupolar moment (slightly higher than ^{27}Al) can

631   be quite sensitive to the local atomic structure, even at low concentrations. Future work

632   on Sc^{3+} may similarly contribute to our understanding Al^{3+} incorporation in other

633   minerals and may extend to other larger rare earth elements as well.

634   Many of the results presented here, particularly on kinetic and temperature

635   effects, are preliminary but suggest interesting prospects for potentially unique and useful

636   future studies. Going beyond substitution mechanisms addressable with ^{27}Al and ^{45}Sc

637   NMR, ^{7}Li, ^{11}B, ^{23}Na, and ^{31}P may be both particularly amenable to future NMR studies of

638   geochemically interesting problems.

21

644   Laboratory) for introducing us to component analysis methods. We also thank two

645   anonymous reviewers for thoughtful responses and constructive comments.

646

647

648   **REFERENCES**

649   Berry, A.J., O'Neill, H.S.C., Hermann, J., and Scott, D.R. (2007) The infrared signature

650   of water associated with trivalent cations in olivine. Earth and Planetary Science

651   Letters, 261, 134–142, http://dx.doi.org/10.1016/j.epsl.2007.06.021.

652   Bershov, L.V., Gaite, J.-M., Hafner, S.S., and Rager, H. (1983) Electron paramagnetic

653   resonance and ENDOR studies of Cr^{3+}-Al^{3+} pairs in forsterite. Physics and

654   Chemistry of Minerals, 9, 95–101.

655   Coogan, L.A., Saunders, A.D., and Wilson, R.N. (2014) Aluminum-in-olivine

656   thermometry of primitive basalts: Evidence of an anomalously hot mantle source for

657   large igneous provinces. Chemical Geology, 368, 1–10,

658   http://dx.doi.org/10.1016/j.chemgeo.2014.01.004.

659   Davis, M.C., Brouwer, W.J., Lipton, A.S., Gan, Z., and Mueller, K.T. (2010)

660   Characterization of cation environments in polycrystalline forsterite by ^{25}Mg MAS,

661   MQMAS, and QCPMG NMR. American Mineralogist, 95, 1601–1607,

662   http://dx.doi.org/10.2138/am.2010.3403.

663   Evans, T.M., O'Neill, H.S.C., and Tuff, J. (2008) The influence of melt composition on

664   the partitioning of REEs, Y, Sc, Zr and Al between forsterite and melt in the system

665   CMAS. Geochimica et Cosmochimica Acta, 72, 5708–5721,

666   http://dx.doi.org/10.1016/j.gca.2008.09.017.

667   Flemming, R.L., Terskikh, V., and Ye, E. (2015) Aluminum environments in synthetic

668   Ca-Tschermak clinopyroxene ($CaAlAlSiO_6$) from Rietveld refinement , ^{27}Al NMR ,

669   and first-principles calculations. American Mineralogist, 100, 2219–2230,

670   http://dx.doi.org/10.2138/am-2015-5348.

671   Grant, K.J., and Wood, B.J. (2010) Experimental study of the incorporation of Li, Sc, Al

672   and other trace elements into olivine. Geochimica et Cosmochimica Acta, 74, 2412–

673   2428, http://dx.doi.org/10.1016/j.gca.2010.01.015.

674   Iuga, D. (2011) Double-quantum homonuclear correlations of spin I=5/2 nuclei. Journal

675   of Magnetic Resonance, 208, 225–234, http://dx.doi.org/10.1016/j.jmr.2010.11.007.

676   Jost, K., Ziemer, B., and Seydel, R. (1977) Redetermination of the structure of β-

677   dicalcium silicate. Acta Crystallographica, B33, 1696–1700.

678   Kim, N., Hsieh, C., and Stebbins, J.F. (2006) Scandium coordination in solid oxides and

23

679   stabilized zirconia: ^{45}Sc NMR. Chemistry of Materials, 18, 3855–3859.

680 Kim, N., Stebbins, J.F., Quartieri, S., and Oberti, R. (2007) Scandium-45 NMR of

681   pyrope-grossular garnets: Resolution of multiple scandium sites and comparison

682   with X-ray diffraction and X-ray absorption spectroscopy. American Mineralogist,

683   92, 1875–1880, http://dx.doi.org/10.2138/am.2007.2601.

684 Kohn, S.C., Roome, B.M., Smith, M.E., and Howes, a. P. (2005) Testing a potential

685   mantle geohygrometer; the effect of dissolved water on the intracrystalline

686   partitioning of Al in orthopyroxene. Earth and Planetary Science Letters, 238, 342–

687   350, http://dx.doi.org/10.1016/j.epsl.2005.08.011.

688 MacKenzie, K., and Smith, M. (2001) Multinuclear Solid-State Nuclear Magnetic

689   Resonance of Inorganic Materials, 727 p.

690 Mason, H., Begg, J.D., Maxwell, R.S., Kersting, A.B., and Zavarin, M. (2016) A novel

691   solid-state NMR method for the investigation of trivalent lanthanide sorption on

692   amorphous silica at low surface loadings. Environmental Science: Processes &

693   Impacts, 18, 802–809, http://dx.doi.org/10.1039/C6EM00082G.

694 Mason, H.E., Harley, S.J., Maxwell, R.S., and Carroll, S. a (2012) Probing the surface

695   structure of divalent transition metals using surface specific solid-state NMR

696   spectroscopy. Environmental Science & Technology, 46, 2806–2812,

697   http://dx.doi.org/10.1021/es203733c.

698 Massiot, D., Fayon, F., Capron, M., King, I., Le Calvé, S., Alonso, B., Durand, J.O.,

699   Bujoli, B., Gan, Z., and Hoatson, G. (2002) Modelling one- and two-dimensional

700   solid-state NMR spectra. Magnetic Resonance in Chemistry, 40, 70–76,

701   http://dx.doi.org/10.1002/mrc.984.

702 Mathworks.com (2007) simplisma.m,

703   https://www.mathworks.com/matlabcentral/fileexchange/15391-multivariate-

704   analysis-and-preprocessing-of-spectral-data/content/simplisma.m. Matlabcentral File

705   Exchange.

706 McCarty, R.J. (2016) Minor element distribution and site preference in geological and

707   technological crystals. 209 p. Ph.D. Thesis, Stanford University.

708   https://purl.stanford.edu/hq740dq1933

709 Monakhova, Y.B., Tsikin, A.M., Kuballa, T., Lachenmeier, D.W., and Mushtakova, S.P.

710   (2014) Independent component analysis (ICA) algorithms for improved spectral

711   deconvolution of overlapped signals in ^{1}H NMR analysis: Application to foods and

712   related products. Magnetic Resonance in Chemistry, 52, 231–240,

713   http://dx.doi.org/10.1002/mrc.4059.

714 Neuville, D.R., Cormier, L., Montouillout, V., Florian, P., Millot, F., Rifflet, J.C., and

715   Massiot, D. (2008) Structure of Mg- and Mg/Ca aluminosilicate glasses: ^{27}Al NMR

716   and Raman spectroscopy investigations. American Mineralogist, 93, 1721–1731,

717   http://dx.doi.org/10.2138/am.2008.2867.

718 Neuville, D.R., Ligny, D. De, Cormier, L., Henderson, G.S., Roux, J., Flank, A.-M., and

719   Lagarde, P. (2009) The crystal and melt structure of spinel and alumina at high

720   temperature: An in-situ XANES study at the Al and Mg K-edge. Geochimica et

721   Cosmochimica Acta, 73, 3410–3422, http://dx.doi.org/10.1016/j.gca.2009.02.033.

722 Purton, J.A., Allan, N.L., and Blundy, J.D. (1997) Calculated solution energies of

723   heterovalent cations in forsterite and diopside: implications for trace element

724   partitioning. Geochimica et Cosmochimica Acta, 61, 3927–3936.

725 Shannon, R.D., and Prewitt, C.T. (1969) Effective ionic radii in oxides and fluorides.

726   Acta Crystallographica, B25, 925-946, https://doi.org/10.1107/S0567740869003220.

727 Skibsted, J., Jakobsen, H., and Hall, C. (1994) Direct observation of aluminium guest

728   ions in the silicate phases of cement minerals by ^{27}Al MAS NMR spectroscopy.

729   Journal of the Chemical Society, 90, 2095–2098.

730 Solidstatenmr.com (2017) SIMPLISMA tutorial,

731   http://solidstatenmr.com/analysis.php#SIMPLISMA

732 Stebbins, J.F. (1995) Nuclear magnetic resonance spectroscopy of silicates and oxides in

733   geochemistry and geophysics. In Ahrens, T. (Ed.) A Handbook of Physical

734   Constants, AGU Reference Shelf 2 pp. 303–331. American Geophysical Union.

735 Stebbins, J.F., and Xue, X. (2014) NMR Spectroscopy of Inorganic Earth Materials.

736   Reviews in Mineralogy and Geochemistry, 78, 605–653,

737   http://dx.doi.org/10.2138/rmg.2014.78.15.

738 Stoyanova, R., and Brown, T.R. (2001) NMR spectral quantitation by principal

739   component analysis. NMR in Biomedicine, 14, 271–277,

740   http://dx.doi.org/10.1002/nbm.700.

25

741   Stoyanova, R., Kuesel, A.C., and Brown, T.R. (1995) Application of principal-

742   component analysis for NMR spectral quantitation. Journal of Magnetic Resonance,

743   Series A, 115, 265–269, http://dx.doi.org/10.1006/jmra.1995.1177.

744   Wan, Z., Coogan, L.A., and Canil, D. (2008) Experimental calibration of aluminum

745   partitioning between olivine and spinel as a geothermometer. American

746   Mineralogist, 93, 1142–1147, http://dx.doi.org/10.2138/am.2008.2758.

747   Windig, W. (1997) Spectral data files for self-modeling curve resolution with examples

748   using the Simplisma approach. Chemometrics and Intelligent Laboratory Systems,

749   36, 3–16, http://dx.doi.org/10.1016/S0169-7439(96)00061-5.

750   Windig, W., and Guilment, J. (1991) Interactive self-modeling mixture analysis.

751   Analytical Chemistry, 63, 1425–1432, http://dx.doi.org/10.1021/ac00014a016.

752   Windig, W., Antalek, B., Lippert, J.L., Batonneau, Y., and Bre, C. (2002) Combined use

753   of conventional and second-derivative data in the SIMPLISMA self-modeling

754   mixture analysis approach. Analytical Chemistry, 74, 1371–1379.

755   Zakaznova-Herzog, V.P., Malfait, W.J., Herzog, F., and Halter, W.E. (2007) Quantitative

756   Raman spectroscopy: Principles and application to potassium silicate glasses.

757   Journal of Non-Crystalline Solids, 353, 4015–4028,

758   http://dx.doi.org/10.1016/j.jnoncrysol.2007.06.033.

759   Zhang, F., and Wright, K. (2010) Coupled (H^+,M^{3+}) substitutions in forsterite.

760   Geochimica et Cosmochimica Acta, 74, 5958–5965,

761   http://dx.doi.org/10.1016/j.gca.2010.07.019.

762   ——— (2012) Lithium defects and diffusivity in forsterite. Geochimica et

763   Cosmochimica Acta, 91, 32–39, http://dx.doi.org/10.1016/j.gca.2012.05.034.

764

765

766

767

List of Figure Captions

768

769 **Figure 1.** Backscattered electron image of Al doped forsterite and an Al rich glass visible in triple junction

770 pockets and along grain boundaries. This sample was ground in a zirconia mortar, which added significant

771 ZrO_2 that was concentrated in the glass, increasing its contrast relative to the forsterite and probably leading

772 to an unusually large glass content.

773

774 **Figure 2.** ^{27}Al NMR spectra at 18.8 T of forsterite and enstatite doped with Al (Table 1). The forsterite

775 sample was heated with 910 μg/g, but only 35% of the Al was incorporated into the bulk sample, indicating

776 that 65% of the spectrum is related to impurity phases. In the enstatite spectrum, peaks for a spinel impurity

777 are clearly visible at 69 and 12.2 ppm. Note how the forsterite sample has a peak minimum at the enstatite

778 peak maximum (-1.1 ppm) indicating that although this sample contains impurities, it contains minimal, if

779 any, Al-enstatite. 0.1 s delay time.

780

781 **Figure 3.** ^{27}Al NMR spectra at 14.1 T of 5 forsterite samples illustrating their variability (Table 1), and the

782 three components determined by SIMPLISMA. Component 1 originates from Al in forsterite, component 2

783 from unreacted spinel, and component 3 from Ca-Mg aluminosilicate glass, all of which can individually be

784 identified in most of the experimental spectra above.

785

786 **Figure 4.** ^{27}Al NMR spectra at 14.1 T of one sample of forsterite heated first at 1500, then at 1200 ˚C

787 (Table 1). Peak height normalized to the lowest frequency AlO_6 peak. Note how the intensities of the

788 forsterite AlO_4 and AlO_6 peaks are larger in the low temperature sample. Pulse delay times of 0.1 s.

789

790 **Figure 5.** ^{27}Al spectra of MgO heated with 1870 μg/g Al for 68 hours at 1600 °C. Collected at 14.1 T, 0.1 s

791 delay times.

792

793 **Figure 6.** ^{27}Al NMR spectra of larnite (belite) heated with 0.53 wt% (Larnite 0.53%) or 0.15 wt% (Larnite

794 0.15%) Al, a simulation of the highest frequency feature, and three SIMPLISMA components. The

795 simulated peak is likely the only Al component originating from larnite. Component 1 replicates the

796 simulated peak, component 2 closely resembles that of Al incorporated in tricalcium silicate ("alite" or

797 "C_3S") and component 3 is very similar to the spectrum of a gehlenite composition glass. The additional

798 features in component 1 relative to the simulation are most likely indicating negative correlation to

799 component 2 (i.e. analyzed samples with component 1 statistically had less component 2) and positive

800 correlation with some signal from glass.

801

802

803   **Figure 7.** ^{45}Sc NMR spectra of Sc^{3+} doped forsterite (middle), the simulation of its primary feature

804   (bottom), and pure Sc_2O_3 (top).

805

806   **Figure 8.** ^{45}Sc spectra of Sc doped periclase (MgO). A very narrow peak originating from Sc^{3+} in an Mg

807   site with nearly cubic point symmetry is visible at 210 ppm. Both samples contain excess Sc_2O_3; in the

808   upper spectrum its spinning sidebands are intense enough to be seen as marked.

809

810

811

812   **Tables**

813   **Table 1.** Labels and synthesis conditions for samples shown in figures.

Figure label	Mineral of interest	Al or Sc source	Intended Al or Sc (μg/g)[a]	Observed Al or Sc (μg/g EPMA)	% in mineral[b]	Temp. (°C)	Hours
Fo-A	forsterite	Spinel	910	320(175)	35	1500	168
Fo-A 1200 °C	forsterite	Spinel	910	-[c]	35	1200	+72[d]
Fo-B	forsterite	γ-Al(OH)$_3$	5450	1150(230)	21	1500	85
Fo-C	forsterite	Spinel	950	320(210)	34	1500	205
Fo-D	forsterite	Spinel	2520	725(120)	29	1500	60
Fo-E 225 hrs	forsterite	Spinel	600	160(70)	27	1550	227
Fo-E 156 hrs	forsterite	Spinel	600	-[e]	27	1550	156
Al-enstatite	enstatite	Al$_2$O$_3$	1.32%	0.68%(0.12)	51	1300	144
Al-MgO	periclase	Al(OH)$_3$ NP	1870	-	-	1600	68
Larnite 0.15%	larnite	γ-Al(OH)$_3$	1500	-	30[f]	1450	61.5
Larnite 0.53%	larnite	γ-Al(OH)$_3$	5300	2100(160)	40	1450	61.5
Sc$_2$O$_3$	Sc$_2$O$_3$	-	-	-	100	1500	16.6
Sc-forsterite	forsterite	Sc$_2$O$_3$	3330	2900(145)	87	1500	192
Sc-MgO 50%	periclase	Sc$_2$O$_3$	50%	500[g]	-	1300	72
Sc-MgO 1.6%	periclase	Sc$_2$O$_3$	1.6%	30[g]	-	1280	72

814

815   [a]Intended bulk composition in μg/g of Al or Sc unless indicated as wt%.

816   [b]The estimated percentage of Al or Sc determined to be within the mineral of interest on the basis of

817   intended synthesis composition and EPMA observed composition.

818   [c]No significant difference in Al composition from that of the parent material (Fo-A) was detected.

819   [d]Heated for an additional 72 hours at 1200 °C beyond that of the parent material (Fo-A).

820   [e]This is the parent material of Fo-E 227 hrs, and was not extensively investigated by EPMA.

821   [f]"% in mineral" estimated using NMR fitting.

822   [g] Sc in MgO roughly estimated from NMR data only.

823

29

824 **Table 2.** NMR peak parameters derived here or reported previously.

Mineral	Site	NMR-observed coordination	δ_{iso} (ppm)	C_Q (MHz)	η	Source[a]
periclase	MgO_6	AlO_6	15.8 ± 0.3	< 0.45	-	
periclase	MgO_6	ScO_6	210 ± 0.5	< 1.5	-	
larnite	-	AlO_4	96.1 ± 0.5	7.1 ± 0.2	0.33 ± 0.05	Skibsted et al. 1994
larnite	Si	AlO_4	94 ± 0.2	5.8 ± 0.13	0.54 ± 0.04	
forsterite	M1	MgO_6	-	5.22	0.97	Davis et al. 2010[b]
forsterite	M2	MgO_6	-	4.31	0.42	Davis et al. 2010[b]
forsterite	M2?	ScO_6	106.5 ± 1.2	9.38 ± 0.28	0.68	

825

826 [a]Source is this work or literature reference cited.

827 [b]C_Q and η determined from simulating a MAS spectra at 18.5 T (Davis et al. 2010).

828

829

830

831

832

833   **Figures**
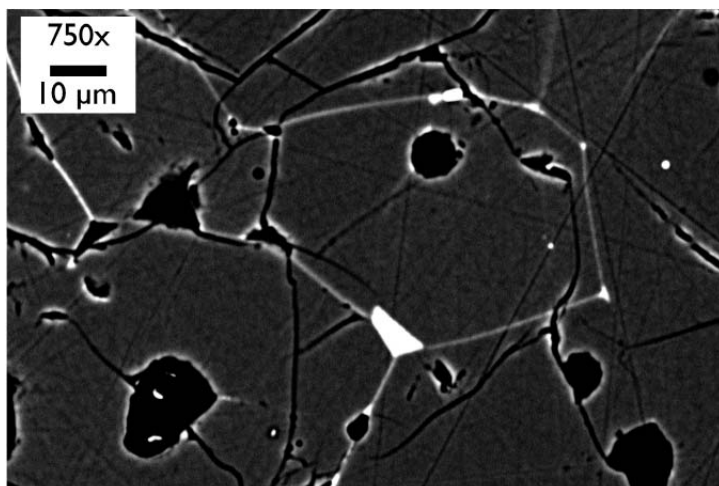
834

835   **Figure 1.** Backscattered electron image of Al doped forsterite and an Al rich glass visible in triple junction
836   pockets and along grain boundaries. This sample was ground in a zirconia mortar, which added significant
837   ZrO_2 that was concentrated in the glass, increasing its contrast relative to the forsterite and probably leading
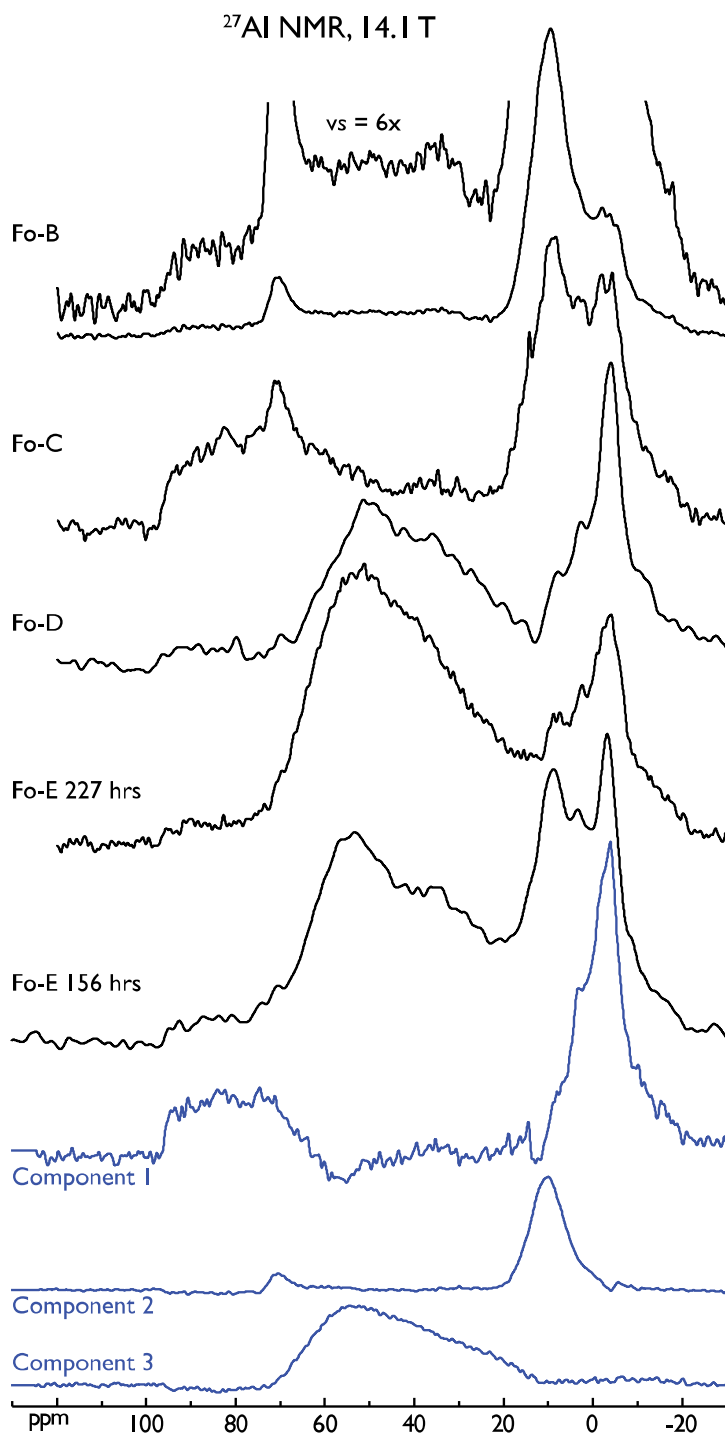838   to an unusually large glass content.

839

840
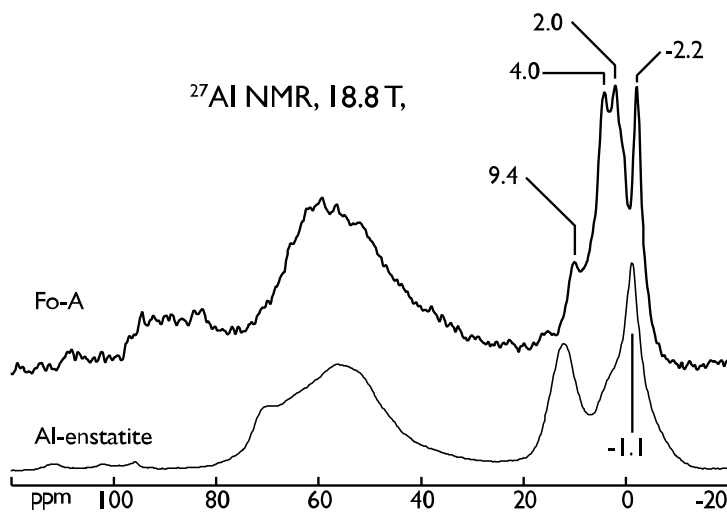
841

842   **Figure 2.** ^{27}Al NMR spectra at 18.8 T of forsterite and enstatite doped with Al (Table 1). The forsterite
843   sample was heated with 910 μg/g, but only 35% of the Al was incorporated into the bulk sample, indicating
844   that 65% of the spectrum is related to impurity phases. In the enstatite spectrum, peaks for a spinel impurity
845   are clearly visible at 69 and 12.2 ppm. Note how the forsterite sample has a peak minimum at the enstatite
846   peak maximum (-1.1 ppm) indicating that although this sample contains impurities, it contains minimal, if
847   any, Al-enstatite. 0.1 s delay time.

848

31

Figure 3. ^{27}Al NMR spectra at 14.1 T of 5 forsterite samples illustrating their variability (Table 1), and the three components determined by SIMPLISMA. Component 1 originates from Al in forsterite, component 2 from unreacted spinel, and component 3 from Ca-Mg aluminosilicate glass, all of which can individually be identified in most of the experimental spectra above.

849
850
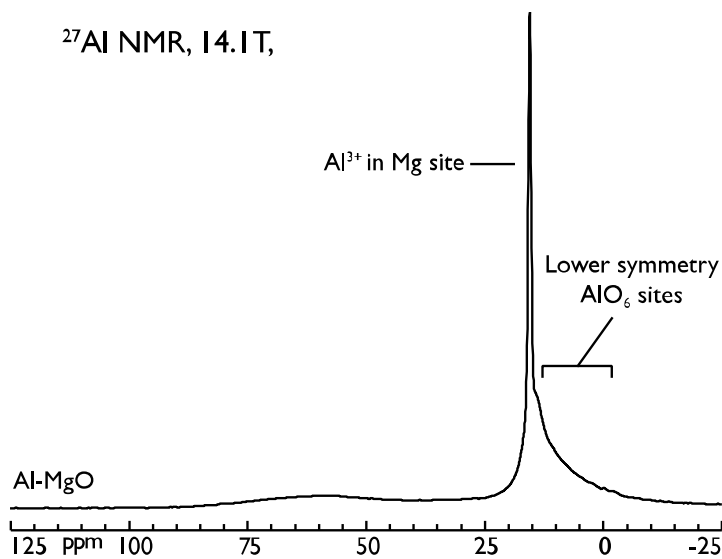851
852
853
854
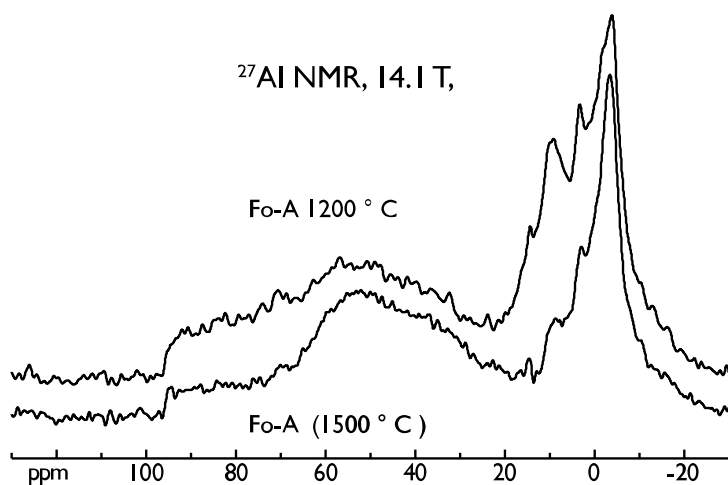
32

Figure 4. ^{27}Al NMR spectra at 14.1 T of one sample of forsterite heated first at 1500, then at 1200 ˚C (Table 1). Peak height normalized to the lowest frequency AlO_6 peak. Note how the intensities of the forsterite AlO_4 and AlO_6 peaks are larger in the low temperature sample. Pulse delay times of 0.1 s.
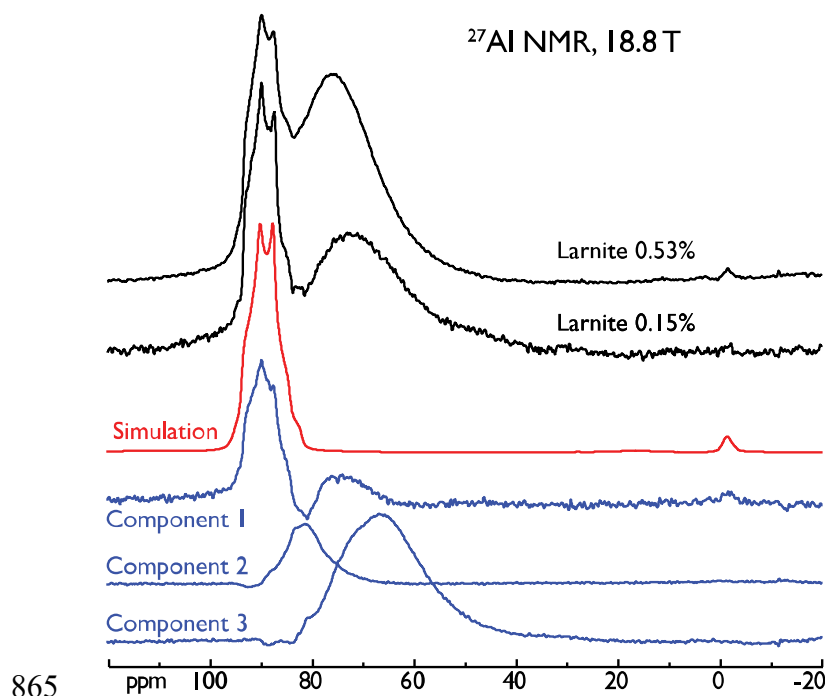

Figure 5. ^{27}Al spectra of MgO heated with 1870 μg/g Al for 68 hours at 1600 °C. Collected at 14.1 T, 0.1 s delay times.

33

865

866 **Figure 6.** ^{27}Al NMR spectra of larnite (belite) heated with 0.53 wt% (Larnite 0.53%) or 0.15 wt% (Larnite

867 0.15%) Al, a simulation of the highest frequency feature, and three SIMPLISMA components. The

868 simulated peak is likely the only Al component originating from larnite. Component 1 replicates the

869 simulated peak, component 2 closely resembles that of Al incorporated in tricalcium silicate ("alite" or

870 "C_3S") and component 3 is very similar to the spectrum of a gehlenite composition glass. The additional

871 features in component 1 relative to the simulation are most likely indicating negative correlation to

872 component 2 (i.e. analyzed samples with component 1 statistically had less component 2) and positive

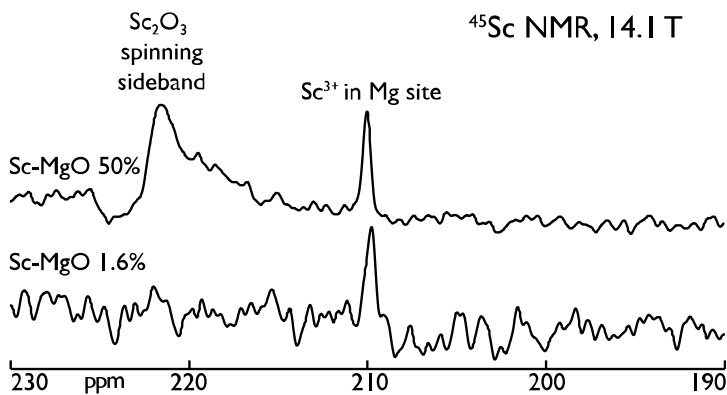873 correlation with some signal from glass.

874

875
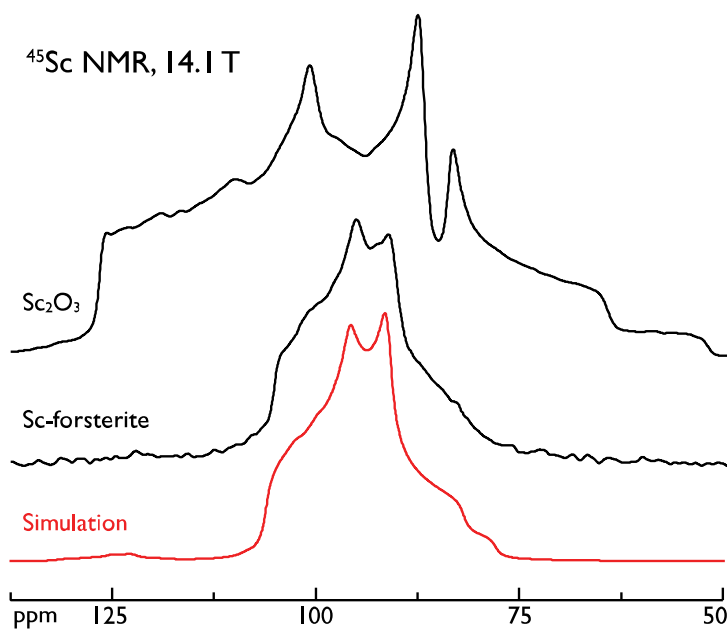
876

Figure 7. ^{45}Sc NMR spectra of Sc^{3+} doped forsterite (middle), the simulation of its primary feature
(bottom), and pure Sc_2O_3 (top).

879

880

Figure 8. ^{45}Sc spectra of Sc doped periclase (MgO). A very narrow peak originating from Sc^{3+} in an Mg
site with nearly cubic point symmetry is visible at 210 ppm. Both samples contain excess Sc_2O_3; in the
upper spectrum its spinning sidebands are intense enough to be seen as marked.

884

35